Article

The Effect of Dimple Overlap on Wettability and Corrosion Resistance of Laser-Textured Stainless Steel

Deyuan Lou [1], Enkang Liang [1], Pengjian Chen [1], Guodong Jiang [2], Lishi Wang [2], Laiqing Guan [1], Yutao Wang [3] and Dun Liu [1,*]

[1] Laser Group, School of Mechanical Engineering, Hubei University of Technology, Wuhan 430068, China; loudeyuan@hbut.edu.cn (D.L.); 102010076@hbut.edu.cn (E.L.); cpg389246@163.com (P.C.); glqdavin@163.com (L.G.)

[2] Hubei Provincial Key Laboratory of Green Materials for Light Industry, Hubei University of Technology, Wuhan 430068, China; jgd66@163.com (G.J.); lswang@mail.hbut.edu.cn (L.W.)

[3] Shanghai Key Laboratory of Laser Beam Micro Processing, Shanghai Institute of Laser Technology, Shanghai 200233, China; fandy459091542@163.com

[*] Correspondence: dun.liu@hbut.edu.cn

Abstract: During the laser surface texturing process, scanning overlap is usually misused, because it cannot only be dimple overlap, but also can be laser spot overlap. Experiments were conducted to investigate the relationship between laser spot overlap and dimple overlap during laser surface texturing. Moreover, the effect of dimple overlap on the laser textured microstructures, wettability, and corrosion performances of stainless steel was analyzed. The results have shown that, due to changing radiation conditions, the dimple diameter and dimple overlap varied in a non-linear way with the increase in laser spot overlap. Furthermore, the variation of dimple overlap rather than laser spot overlap had a direct effect on roughness, wettability, and corrosion resistance. When the dimple overlap was greater than 55%, the surface reached the superhydrophobic state and the maximum apparent contact angle was 162.6°. When the dimple overlap was 83.52%, due to passivation layer formed by laser remelting deposition and oxides compaction, corrosion current density was 2.8×10^{-8} A·cm^{-2}, which was 4% of the original value. Consequently, it was determined that it is easier to control the surface roughness, wettability, and corrosion resistance via dimple overlap rather than laser spot overlap in laser surface texturing process.

Keywords: laser surface texturing; dimple overlap; roughness; wettability; corrosion

1. Introduction

The roughness is a vital material surface characteristic, which significantly affects the adhesion between the material and either the paint or a coating. Additionally, it affects the material wettability and corrosion resistance [1]. Thus, surface roughness significantly influences the general and pitting corrosion of stainless steel [2].

Lasers had the advantages of high processing speed, high processing accuracy, low thermal deformation and material savings in the processing of products due to their high degree of coherence, directionality and intensity. Among the group of methods, laser surface texturing (LST) was adopted to modify the surface roughness of materials since it can affect the wear [3], wettability [4–7], condensation [8], paint appearance [9], biofunctionalization [10], and waveguide properties [11]. A super-hydrophobic surface (SHS) was obtained on AISI304 stainless steel via a picosecond LST (patterning) technology; and the anti-biofouling performance was improved by the laser-induced micro-nano structures [4]. Further, the Al alloy wettability was successfully modified from hydrophilic to hydrophobic by pulsed LST and post treatment [5,6]. LST could improve condensation on surface heat transfer and reduce water retention in heat exchanger systems [8]. The incorporation and use of surface wettability modification in energy systems has a lot of potential.

However, the durability and stability of hydrophobized surfaces prepared by spontaneous adsorption remains a challenge [7]. Next, the relationship between the nanosecond laser processing parameters and the features of textured micro-grooves in LST was established, which improved the osteoblast adhesion and proliferation of Ti alloys [9]. LST is a clean, versatile, high-temporal, highly efficient, and chemical-free method to modify the surface roughness/chemistry in biomedical polymer implant modification [10]. LST can improve the roughness of laser waveguide surface/wall, and can decrease the pump threshold and increase the laser efficiency [11].

When the LST was applied, micro dimples appeared, meaning that the laser spot overlap (LSO) had a vital role in determining both surface microstructures and material morphologies. It was found that the probability of stress concentration and mutation in the overlap area was increased [12]. Furthermore, with an increase in surface roughness, the stability of metal pitting corrosion potential decreased, and the sensitivity of pitting corrosion increased [13]. The effect of laser texturing parameters on surface roughness [14] and material properties was, therefore, of interest. Current research on the use of lasers to modify roughness was divided into two areas. On the one hand, it focused on the effect of laser parameters on surface roughness. On the other hand, it considered the effect of spot lap rate on material properties. However, studied on surface microweaving were mainly divided into two types: discrete and continuous texture [15]. No scholars had yet conducted a comprehensive study of microweaving from discrete to continuous states.

Some scholars selected three typical texture patterns in ns LST, both in pulse overlap and scanning overlap [16]. They found that ns LST can improve the appearance of galvanized steel sheet paint by imprinting dies, also improving the roughness transfer capability. However, types of patterns about overlap mechanism were not covered in the study. The SHS was produced on carbon steels using ns LST, and the textured steel specimen was further modified by low surface energy material [17]. It was found that the pulse pitch-to-spot diameter of the drawn unit circle adopted in the laser process had a critical role in the textured surface morphology, specifically affecting the corrosion resistance. Further, designed unit shapes are not the smallest textured LST units. A wettable surface was created on thin stainless steel foils using LST [18]. The ns laser with various laser fluences and scan line separations was used and all the cross lines in high density of pulses were drawn. Similarly, titanium was LST to improve its wettability and optical properties by using high-density laser pulses. The specimens were hexagonal honeycomb units that were machined using ns LST [19]. Simultaneously, we found that the surface roughness does not grow linearly with the increase in the LSO in laser micro-nano texture processing. Although several studies on laser surface texturing were carried out, both the arrangement and design of the unit in laser processing were not studied systematically.

In this study, therefore, an application of a nanosecond pulsed laser is proposed and demonstrated for texturing of 316L stainless steel. The influence of dimples with different overlap rates on the induced nanoscale textures is systematically investigated. The effect of DO on the surface roughness, wettability transition, and corrosion resistance was investigated using SEM, XPS and electrochemical workstation studies.

2. Materials and Methods

The raw materials (8 mm × 8 mm × 1 mm) used in this experiment were prepared by a wire-electrode cutting machine and were cut from AISI 316L stainless steel plate.

The AISI 316L stainless steel specimens were ground using 200 grit abrasive papers. Before and after the laser processing, samples were cleaned in anhydrous ethanol for 10 min; an ultrasonic bath was used, and specimens were dried using a cold wind. The average substrate roughness parameters were as follows: R_a = 0.283 µm, R_z = 5.274 µm, the highest contour peak value was 3.56 µm, and the lowest trough depth was −2.36 µm.

The LST is generally considered a pollution-free and efficient technology to produce high-precision micro functional surfaces. Aiming to obtain the laser surface micro-nano

texturing, samples were treated by a nanosecond laser (SPI's SP-070-A-EP-Z-B-Y 70 W). The laser processing parameters are given in Table 1.

Table 1. The parameters of laser processing.

Wavelength (nm)	Pulse Width (ns)	Repeat Frequency (Hz)	Single Pulse Energy (J)	Scanning Speed (mm/s)
1064	240	70×10^3	874.3×10^{-6}	1400~9100

The laser beam diameter was 47.5 µm and its profile was Gaussian in shape. As shown in Figure 1, the laser scanning path was an isosceles right-angle scanning method. The distance between spots was equal to the row spacing, that is, the pulse overlap was equal to the scan overlap. Thus, the laser overlap rate δ can be calculated using Equation (1).

$$\delta = \left(1 - \frac{L}{D}\right) \times 100\% = \left(1 - \frac{v}{fD}\right) \times 100\% \tag{1}$$

where δ is the LSO percentage, L is the distance between two scanning paths (mm), D is the spot diameter (µm), f is the repetition frequency (kHz), and v is the scanning speed (mm/s)
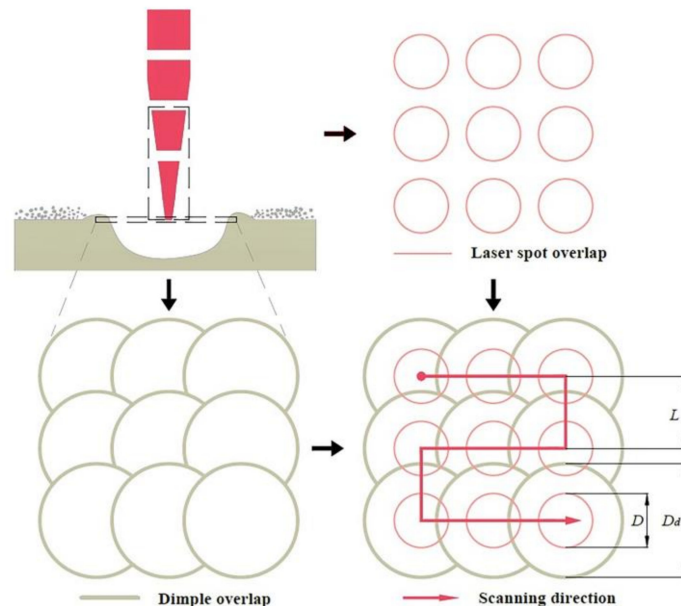

Figure 1. The schematic diagram of the laser surface texturing.

Using various LSO rates, uniform micropores were produced on the stainless-steel sample surfaces.

To analyze the relationship between the LSO rate and surface roughness of stainless-steel surface textured by short-pulse laser, the dimple diameter D_d was introduced to replace the laser spot diameter D. At the same time, the overlap rate of dimples under the equal waist method was introduced in Equation (2) as follows:

$$\delta_d = (1 - \frac{L}{D_d}) \times 100\% = (1 - \frac{v}{fD_d}) \times 100 \tag{2}$$

In Equation (2), δ_d is dimple overlap rate, D_d is dimple diameter (µm).

Before the contact angle test, textured steel plates were placed in an open oven with a constant temperature of $120 \pm 1\,°C$ and kept there for 24 h.

Morphologies of laser textured surfaces were characterized using an optical microscope and a scanning electron microscope (JSM-6390 LV, JEOL Ltd., Tokyo, Japan). Multipoint arc fitting was carried out using imageJ under the OM images. When the dimples

were not densely lapped, the average diameter was measured by fitting the whole circle at multiple points, and after the dimples were densely lapped, the dimple diameter was derived and averaged using partial arc fitting of the dimples. The sample surface roughness was measured using a Contour GT-K0 surface profilometer, allowing the authors to collect the 3D morphologies. The surface contact angles were tested using a water contact angle measuring instrument (Dropmeter TM Experience A-300, Maist Co. Ltd., Ningbo, China). Potentiodynamic curves were depicted for the four epoxy resin sealed samples in a 3.5 wt.% NaCl aqueous solution. The experimental apparatus used in this study was a Zennium electrochemical workstation with a frequency range from 10 µHz to 4 MHz. Moreover, larger samples (9 cm^2) were used for corrosion testing to facilitate data collection and analysis. Samples were cleaned using deionized water and were dried naturally before the test. When the potentiodynamic curves were measured, four samples were soaked into a 3.5 Wt.% NaCl aqueous solution at room temperature for 30 min. The electrochemical measurement method for the three-electrode system was adopted, with a reference saturated calomel electrode. The specific parameters for each of the four samples are listed in Table 2.

Table 2. DO rate of the samples for corrosion studies.

No.	0#	1#	2#	3#
δ_d (%)	316L Stainless Steel	−14.35	34.02	83.52

3. Results

3.1. The Effect of LSO on the Dimple Sizes

The optical microscopic images of samples with different spot overlap percentages after LST were shown in Figure 2. As the LSO rate δ gradually increased, the micro-dimples ("crater") affected by the laser went from discrete to dense.
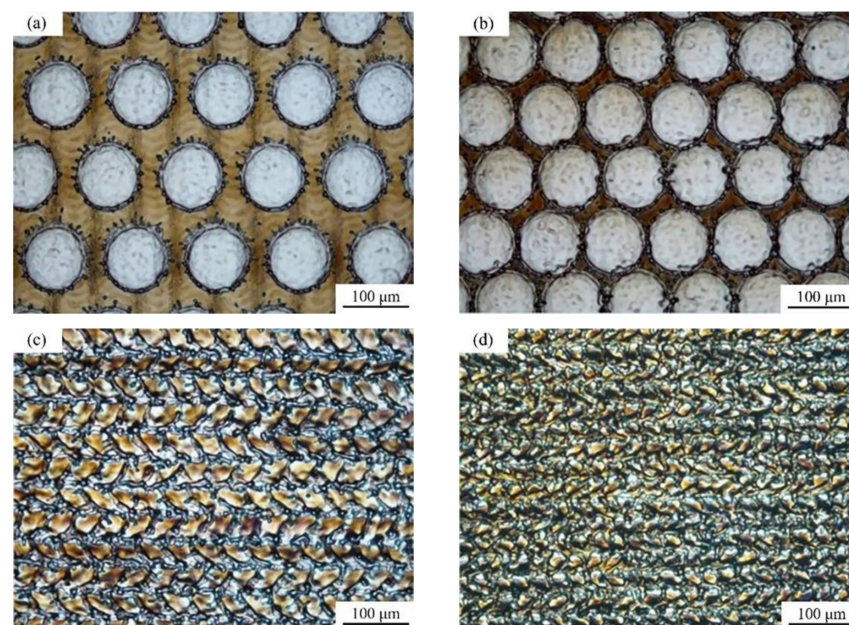

Figure 2. OM images of the sample with different LSO percent: (**a**) −160%; (**b**) −100%; (**c**) 20%; (**d**) 40%.

Sample surface images obtained at different LSO rates are shown in Figure 3. The relationship between the micro-dimple size and LSO rate can be divided into three stages:

- In the first stage (δ ranging from −160% to −40%), the diameter of a micro dimple (using the inner arc as a measurement) is maintained at approximately 108 µm;
- In the second stage (δ ranging from −30% to 20%), the micro dimple diameter increased approximately 110.6 µm. With the increase in the LSO, the irradiation distance

of the pulse spot was shortened, and the heat deposited per unit area increased. As heat accumulated on the surface, the thermal stress would exceed the yield strength, resulting in plastic deformation and larger dimples [20];

- In the third stage (δ ranging from 30% to 60%), micro dimple size increased to approximately 115.3 μm. The higher overlap rate increased the energy of laser interaction per unit area, sharply increasing the surface temperature. When the surface temperature reached the stainless-steel boiling point, the steel will vaporize and cause a sharp increase in the dimple size.
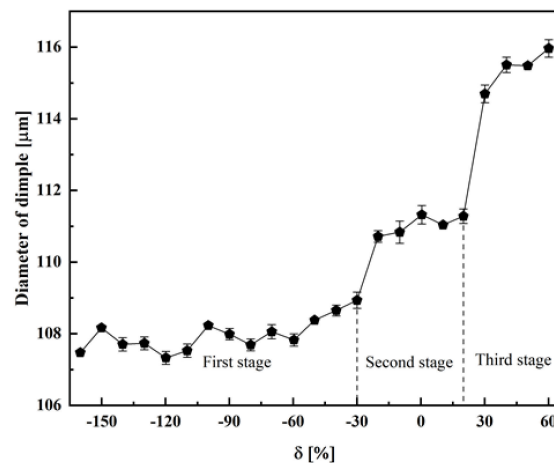

Figure 3. Dimple diameter variation with different LSO rates.

Finally, remaining factors such as deeper laser irritation into stainless steel, larger molten pool volume, and more plasma blasting area also have a significant influence on the pulse interaction.

Additionally, it was found that the size of micro-dimples was not only related to LSO but also to the laser power [21]. Similarly, it was found that when laser power is relatively small, the micro-dimple sizes increase with the laser power [22]. However, once laser power reaches the critical value, the change of micro-pit size tends to either grow slowly or remain stable.

According to Equation (2), the dimple overlap rate was affected by scanning speed and dimple diameter, which was different from the LSO rate trend. The dimple overlap rate was calculated by including the diameter of a dimple in stages. The relationship between the DO rate and the LSO rate is shown in Figure 4.
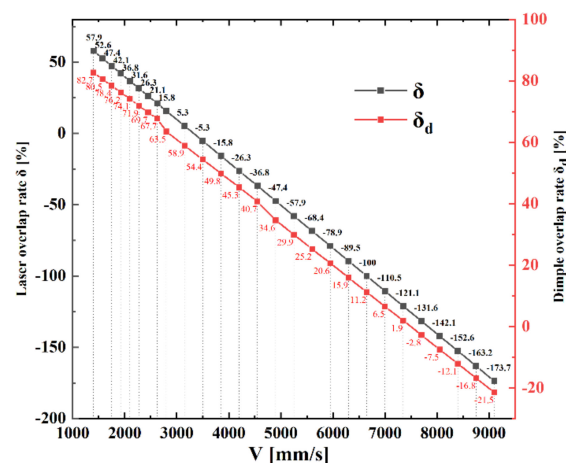

Figure 4. Scanning speed and corresponding LSO rate and DO rate.

3.2. The Effect of DO on the Microstructure and Roughness of Laser Textured Surface

The relationship between DO and surface roughness of stainless steel was shown in Figure 5. The surface roughness first increased during the first stage, followed by an increase in smoothness; however, the overlap between the two places decreased slightly near 7.5% and 29.9%. In the second stage, surface roughness tends to go upwards in overall trend, except for the DO near to 49.8% or 63.5%. In the third stage, the surface roughness generally declines from the peak. If DO continues to grow further, the steel plate will be heated, which will cause deformation.
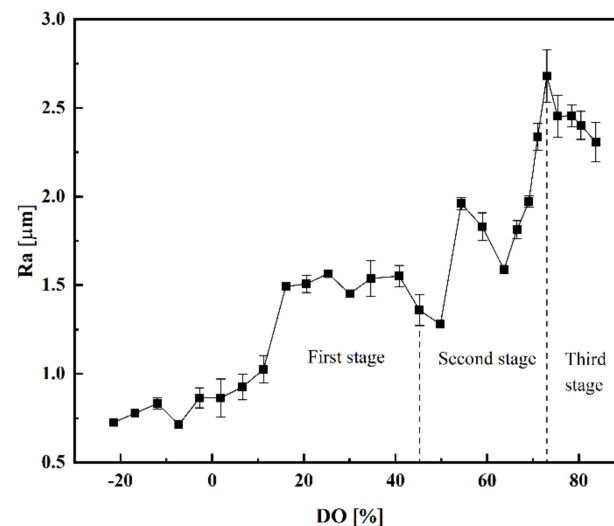

Figure 5. Surface roughness variation under different DO rates.

Combined with the analysis of the dominant laser micro dimple factors in stainless steel, the process of changing the surface roughness was divided into three stages aiming to analyze the effect of DO on surface roughness.

3.2.1. First Stage—A Discrete Condition of Dimples Is Dominant

In the first stage, the dominant factor for textured surface roughness was the discrete dimple degree. The dimples on the stainless-steel surface were discrete when the DO was −21.5%. The main type of laser damage was single pulse damage. According to Figure 2, a single pulse bombards the sample to form burrs on the dimple edges. The 3D surface roughness profile and the schematic diagram of various overlap dimples are given in Figure 6.

When the overlap rate was below −7.5%, the dimples are in a discrete state. With the increase in the overlap rate, the dimples will gradually merge, and the surface roughness slowly increases. However, when the DO increases to −7.5%, the dimples become tangent to each other. During the processing, the latter pulse forms a dimple, and the burr of the previous dimple was removed. In turn, the surface roughness was decreased at this condition. The 3D surface profile of this overlap condition sample was shown in Figure 6a. When the DO was 29.9%, the dimple shapes were similar to −7.5% of the sample—these dimples were tangent, as shown in the red circle in Figure 6d, resulting in surface roughness decrease. The 3D surface profile is shown in Figure 6b. Hence, the increase in surface roughness was observed at first, followed by a smooth period. The R_a decreased slightly as DO near to 7.5% or 29.9%, respectively. The SEM images of the various overlap dimples are shown in Figure 7. As shown in Figure 7a,b, owing to overlap, the change takes place from the grid ring array.
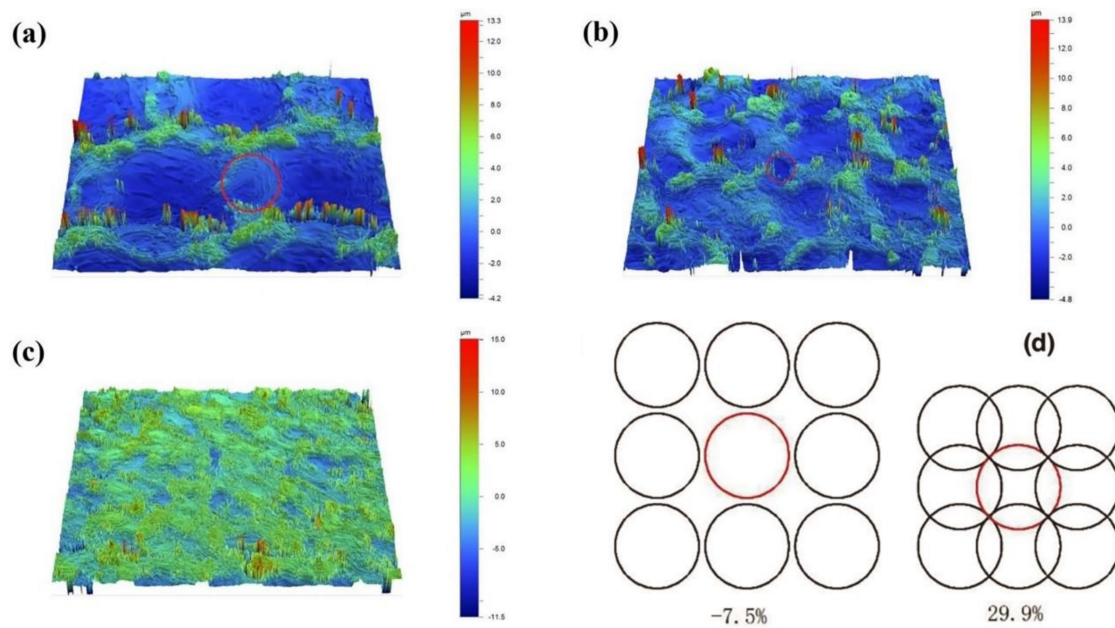
Figure 6. Three-dimensional surface profile of laser textured stainless steel with various DO rates: (**a**) −7.48%; (**b**) 29.9%; (**c**) 82.7% and schematic diagram of dimples with different DO rates (**d**).
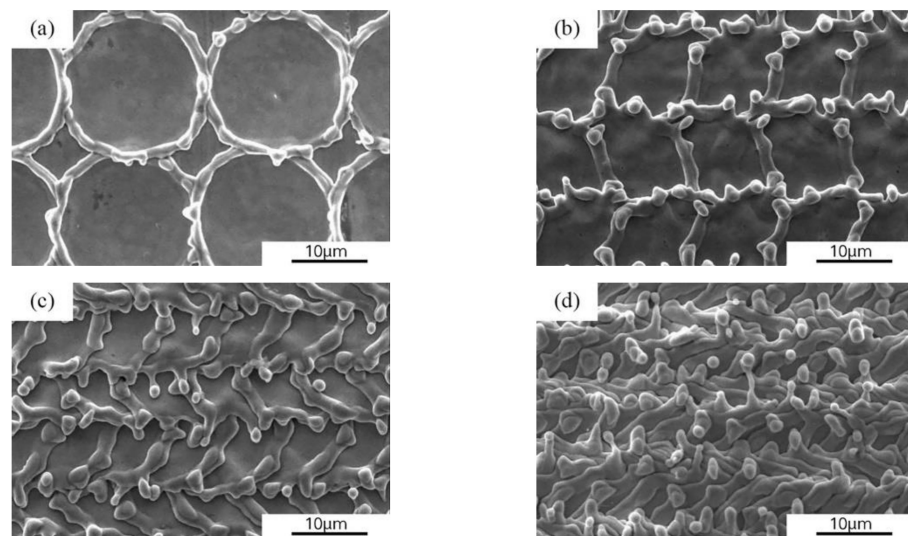

Figure 7. SEM images of stainless-steel surfaces with different DO rates: (**a**) −20%; (**b**) 30%; (**c**) 50%; (**d**) 70%.

3.2.2. Second Stage—The Minimum Area Proportion Is Dominant

The roughness R_a was selected as the evaluation parameter for the surface roughness; it can be calculated by the following Equation (3):

$$R_a = \frac{1}{A_0} \sum_{i=1}^{n} |S_i(N_i - N_{min})| h \tag{3}$$

where A_0 is the area; h is a single-pulse radiation dimple depth; N_i is a pulse number; *Nmin* is the minimum pulse number; *Si* is the ratio between the corresponding area of the N_i pulse number and the total area.

The schematic diagram of dimples in the second stage was shown in Figure 8, and Table 3 includes the statistics of N_i and S_i. Furthermore, Table 3 also shows the surface roughness for various dimple overlaps per unit of area. The N_i and S_i data in Table 3 were

substituted into Equation (3) to find surface roughness. The results are shown in Table 4 and are ordered as follows: $R_a74.1\% > R_a54.4\% > R_a63.5\% > R_a40.7\% > R_a49.8\%$, which is consistent with the indications shown in Figure 5. The calculation of roughness was based on the bottom area, under the condition of smooth bottom surface. Thus, the rate of the total area occupied by the bottom to per unit area was called occupancy area rate (Smin). The larger the Smin, the smaller the Ra. As the DO rate increased from 54.4% to 63.5%, the Smin grew from 1.48% to 33.35%, causing the R_a drop from 1.515 h to 1.2944 h.
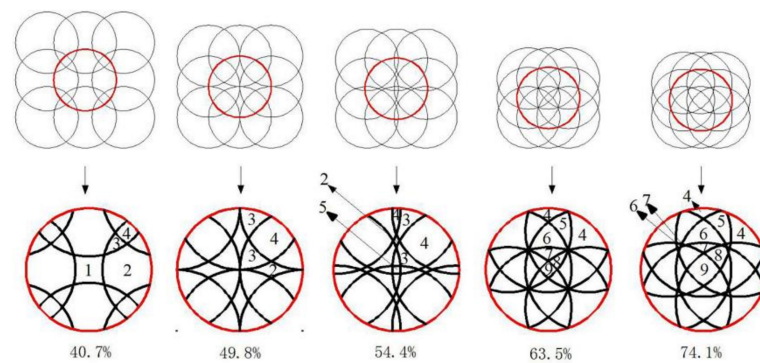

Figure 8. Schematic of laser texturing dimple shape with DO rate of 40.7%, 49.8%, 54.4%, 63.5% and 74.1%.

Table 3. The various shapes data with a different DO rate.

DO Rate δ_d (%)	Numbers of Laser Spot N_i/Occupancy Area Rate S_i (%)								
	1	2	3	4	5	6	7	8	9
40.7	7.81	62.83	20.31	9.05	/	/	/	/	/
49.8	/	17.93	45.54	36.53	/	/	/	/	/
54.4	/	1.48	46.35	51.6	0.52	/	/	/	/
63.5	/	/	/	33.35	28.67	20.78	8.19	5.45%	2.56
74.1	/	/	/	21.81	34.79	21.66	5.54	11.32	4.88

Table 4. Surface roughness of samples with various DO rates.

δ_d(%)	39.25	50	53.27	68.4	71.96
R_a (μm)	1.286 h	1.186 h	1.512 h	1.2944 h	1.644 h

When the DO reached 49.8%, the pulse duration type in a different region (indicated by red circles in Figure 8) will be reduced. There were four types of pulse duration when the overlap equaled 40.7%. However, when the DO was 49.8%, there were only three types and R_a was reduced as well. Furthermore, as can be seen in the SEM images (see Figure 7c,d), more micron-sized mastoids grow as the overlap increases. There were nano-sized clusters on the mastoid and, with the increase in DO, more nano-structures appeared on the laser texture surface.

3.2.3. Third Stage—The Melting and Vaporization/Plasmablast of Dimples Is Dominant

Figure 6c provides an overview of 3D profile images of the third stage. Generally, it is believed that the short-pulse laser exposes to metal will produce a thermal effect through melting vaporization and plasma effect. When the DO grew up to 74.1%, the number of pulses on the surface was more than or equal to four. After that, the interaction area was concentrated, and the neighbor pulse interval was shortened. Additionally, the degree of vaporization and plasma blasting increased, causing roughness to grow to the critical peak point of Ra.

Moreover, the laser pulse radiation energy density in the non-gasified region was higher than the steel melting threshold and the main damage to the sample surface was melting. The melted part with a high radius of curvature would flow to the lower ones; thus, the curvatures on the surface tended to be consistent [23]. Furthermore, the plasma effect of the laser pulse was strengthened during this period, meaning that the surface roughness decreases after reaching its peak point in the third stage.

3.3. The Effect of DO on the Wettability of Textured Stainless Steel Surfaces

The rough surface structure has a critical influence on the wettability of solid surfaces, meaning that the microstructure textured on the surface can change it [24]. Studies have shown that, due to the effect of rough microstructures and nanoclusters, a solid surface has a large contact area with the liquid [25]. The relationship between the apparent contact angle θ_w and the intrinsic contact angle θ_0 of a smooth surface can be calculated by the following Equation:

$$\cos \theta_w = r \cos \theta_0 \tag{4}$$

In Equation (4), r is the roughness factor, which represents the ratio between the actual area and the projected area of the droplet in contact with the solid surface. The intrinsic contact angle θ of a smooth surface is constant, while the apparent contact angle θ_w is related to roughness and microstructure. When θ is greater than 90°, θ_w is greater than θ_0 and increases with the increase of r. The increase of roughness factor r can make the hydrophobic surface more hydrophobic and the hydrophilic surface more hydrophilic.

The roughness factor r is obtained according to the Wenzel theory [26], which introduces it to describe the roughness of surface microstructures. It is defined as the ratio between the real surface area *Asl (true)* and the projected surface area *Asl (apparent)*:

$$r = \frac{Asl(true)}{Asl(apparent)} = \begin{cases} 1 + \frac{\pi h (\csc\varphi + \cot\varphi)(b - h\cot\varphi)}{(l+b)^2} & , \text{DO} < 0 \\ 1 + \frac{4h \sum_{i=1}^{n} |S_i(N_i - N_{min})|}{l} & , \text{DO} \geq 0 \end{cases} \tag{5}$$

When the DO > 0%, where l is the single dimple ring diameter, h is the dimple depth, b is the distance between two adjacent dimples, and φ is the dimple structure dip angle. The schematic diagram of the rough surface structure was given in Figure 9. In this experiment, the dimples were evenly distributed across the stainless-steel surface. The square surrounded by dashed lines is taken as a periodic area.
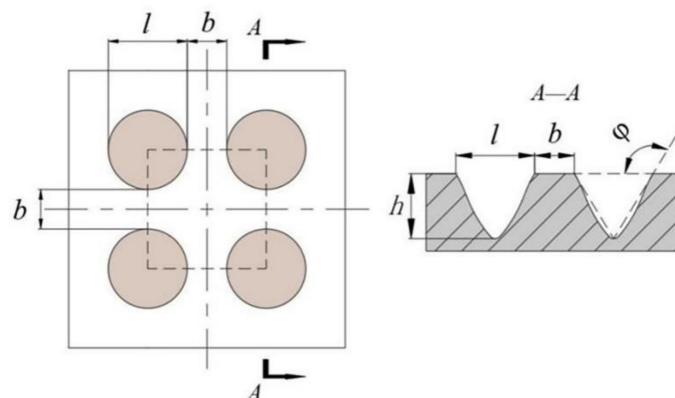

Figure 9. Schematic diagram of rough surface structure.

When the DO ≥ 0%, the dimples begin to lap each other, combined with the idea of Equation (3), where *Ni* is a pulse number; *Nmin* is the minimum pulse number; *Si* is the ratio between the corresponding area of the *Ni* pulse number and the total area.

The dimple width Dd and the dimple depth h were measured by the Contour GT-K0 surface profilometer. φ is calculated as follows

$$\varphi = \pi - \tan^{-1} \frac{2h}{l} \tag{6}$$

For the water contact angle measurements, a droplet size of 5 μL was chosen by means of an OCA15plus optical tester. The surface wettability of the sample was assessed using a contact angle measuring instrument (Dropmeter TM Experience A-300). The intrinsic contact angle θ_0 of the original sample, surface was approximately 100°.The effects of the DO rate on the textured steel surface water contact angle are shown in Figure 10. It can be seen from Figure 9 that the apparent contact angle θ_w firstly increases with the growth of the DO rate, which is followed by a decrease. When the DO was 55%, the water contact angle reached 162.6°, meaning that it was in a superhydrophobic state. When the overlap rate was −25% to 0%, according to Equation (5), r increased slowly with the decrease in dimple distance. When the DO was 0–55%, according to Equation (5), the roughness factor r is related to the number of dimples overlapping per unit area N and the proportion of the overlapping area as well as the single pulse depth h. Again, as the dimple's distance d decreases, the roughness factor r increases. According to Equation (4), when the roughness factor r increased, the θ_w increases. Furthermore, for the DO rate from 55% to 85%, the minimum dimple area decreased with the increase in overlap rate, which resulted in the decrease of the dimples depth h. Additionally, the roughness factor r and the θ_w also decreased, while the distance h from the bottom of the dimple to surface decreased with the increase in δ_w, leading to the decrease of roughness factor r, affecting θ_w.
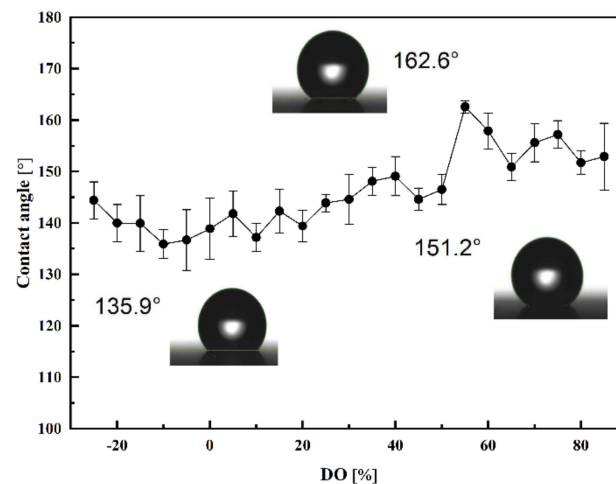

Figure 10. Surface contact angle variation under different DO rates.

Following the laser texturing, the high energy generated by very short laser pulses activates the oxidation process between air and sample, a large amount of oxide is generated, which appears hydrophilic. The subsequent heat treatment process accelerates the deposition of organic matter from the air on the surface of the sample and reduces the surface energy [27]. Simultaneously, due to the existence of surface nanoclusters, the surface wettability changed. Finally, during the laser texturing, liquid-phase blasting and rough-edge stacking result in uneven surface morphology and the fluctuation of the apparent contact angle.

3.4. The Effect of DO on Corrosion Resistance

The potential polarization curves of different DO samples in a 3.5% sodium chloride solution are shown in Figure 11. It is evident that all samples behaved passivation phenomenon, although it was not easily spotted in sample 3#. Furthermore, the corrosion

potential (E_{Corr}), corrosion current density (I_{Corr}), and pitting Vcorrosion electric potential (E_{Pit}) were given for all the samples (please see Table 5).
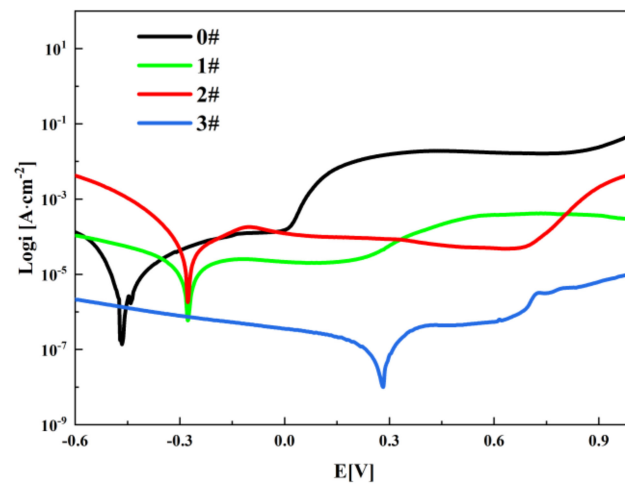

Figure 11. Potentiodynamic polarization curves in 3.5% NaCl aqueous solution.

Table 5. Corrosion parameters of potentiodynamic curves in 3.5% NaCl aqueous solution.

Sample No.	DO Rate/(%)	Corrosion Potential E_{corr} (mV)	Corrosion Current Density I_{corr} (A·cm^{-2})	Pitting Corrosion Electric Potential E_{pit} (V)
0#	/	−472.5	7×10^{-7}	−0.02
1#	−14.4	−277.5	2.8×10^{-6}	0.21
2#	34.0	−271.5	1.1×10^{-5}	0.66
3#	83.5	282.62	2.8×10^{-8}	1.80

All the E_{Corr}, E_{Pit}, and ΔE of laser-textured samples were improved compared to the commercial stainless steel 316L panel. It is clear that the Icorr increases first when the DO grows and declines after the 2# overlap. According to the data above, the corrosion resistance of each sample is ranked from strength to weaker, as shown below. 3#> 0#> 1#> 2#.

The corrosion resistance of the 2# and 1# samples was decreased compared to sample 0#. There were no laser spot overlaps in the 1# sample; dimples formed on the surface were discrete and the laser pulse interval was longer. Thus, cooling time and space were maintained during the laser processing. The 2# sample was in the overlapping stage and the dimples formed on the laser processed sample surface were highly overlapped. The surface was remelted and spattered by the laser-induced plasma; thus, the spattered splatters were produced in the form of dendritic shapes. As shown in Figure 12b,c, during the laser overlap texturing, the steel surface cooled rapidly to solidify, forming the dendritic branches by spattering the induced plasma. Finally, micro-pores of various sizes were observed on both sides of the dendritic. For holes or overlap cavities formed near the dendritic, pitting corrosion was worse along dimple edges. Further, since the galvanic corrosion occurred more frequently at the junction between the oxide and metal matrix, both sides of dendrite splatter branches provided pitting corrosion conditions. The corrosion pits were mainly distributed along the dendritic edge of textured dimples (Figure 12c).
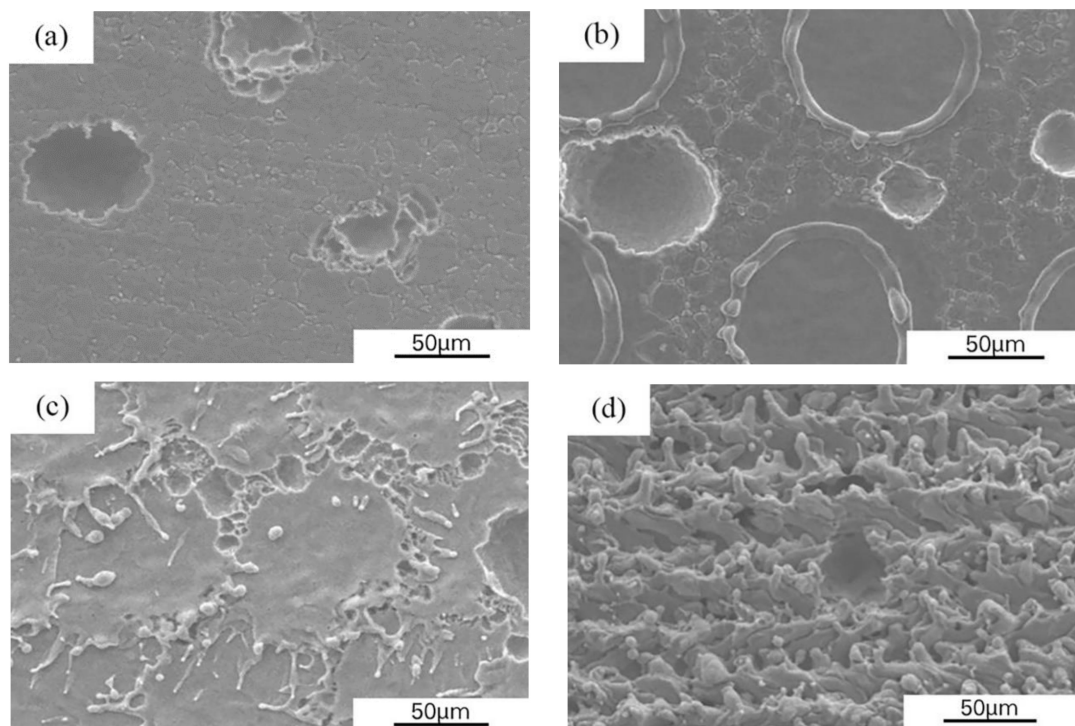
Figure 12. SEM images of samples after corrosion test: (**a**) 0#; (**b**) 1# $\delta_d = -14.35\%$; (**c**) 2# $\delta_d = 34.02\%$; (**d**) 3# $\delta_d = 83.52\%$.

Further, the pitting corrosion was also increased through oxidation. Figure 13 outlines a line scanning spectrum of O elements near sample 2#. It can be seen that the oxidation of the splatter dendritic structure surface was severe and that there was a sudden change in oxygen content (compared to a substrate, as other elements remain unchanged). In a high overlap laser texturing, splatter and oxidation of steel surfaces were strengthened, and after splatter dendritic branches covered most of the steel surfaces, the galvanic corrosion effect was diminished. Therefore, the corrosion resistance of the 3# sample was enhanced.
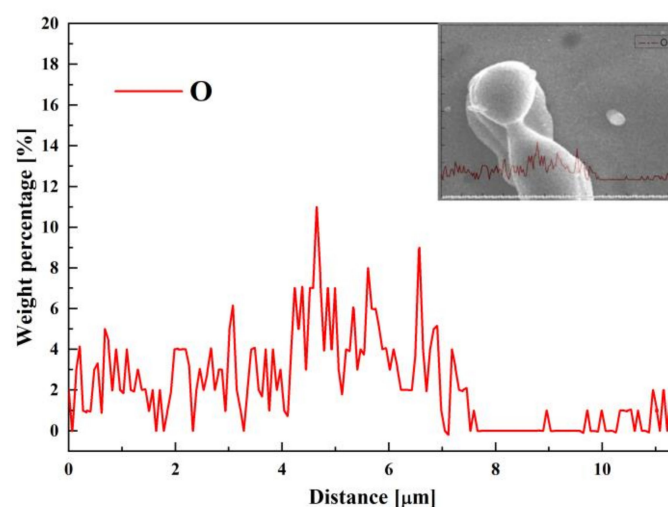

Figure 13. Oxygen element line scanning spectrum cross the sputter of sample 2#.

The surface SEM image following the ultrasonic cleaning with a dilute oxalic acid solution to remove the corrosive cover was given in Figure 14, clearly revealing that small, deep holes remained after pitting corrosion. During the re-melting process, some of these

tiny holes shaped by the front dimples were covered by a splattered mastoid structure due to the latter dimples, thus further improving the pitting corrosion resistance.
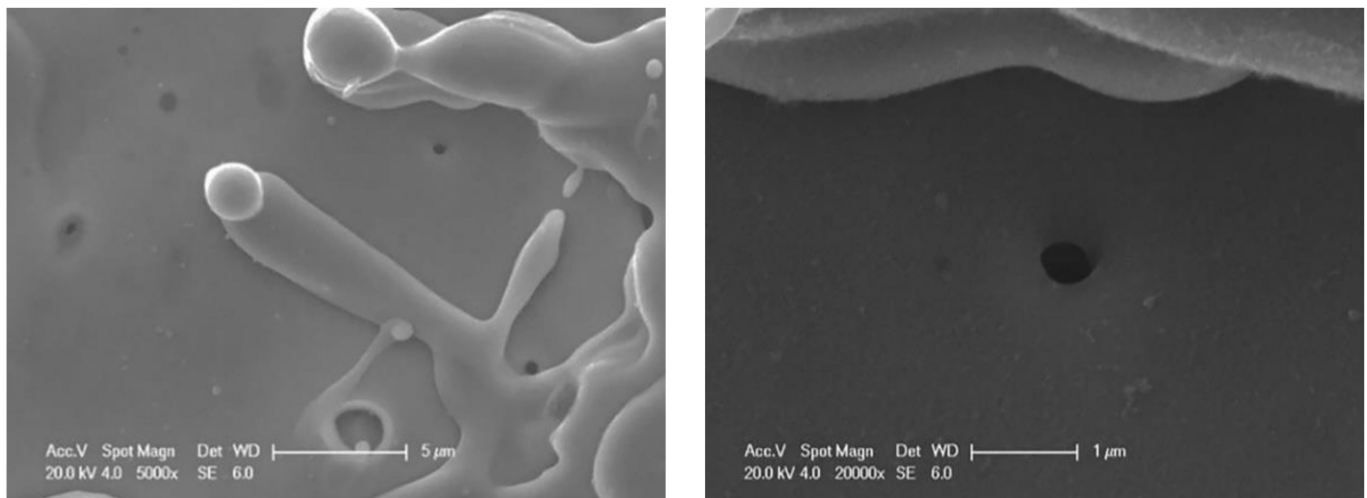

Figure 14. SEM images of the sample surface after ultrasonic etching cleaning.

4. Conclusions

In this study, a nanosecond laser was used to texture the surface of 316L stainless steel. The relationship between the laser spot overlap (LSO) and dimple overlap (DO) was investigated, and the effects of DO on the surface roughness, wettability, and corrosion performance were observed. The DO was found to be the key factor for controlling the surface roughness, wettability, and corrosion resistance in laser surface texturing. Based on the results, main conclusions were drawn as follows:

(1) The size, shape, and microstructure of laser textured steel surface dimples cannot be linearly controlled via the LSO rate. When the LSO rate ranged from −160% to 60%, the dimple diameter was determined not only by the LSO thermal effect but also by the beam power density;

(2) The DO affecting the surface roughness can be divided into three stages, each having different dominant factors. When DO was between −21.5% and 34.6%, R_a firstly increased, which was followed by a flat period. The dominant factor was the degree of dimple dispersion. As DO changed to 40.7~63.5%, R_a has shown an upward oscillation trend. The bottom-to-surface rate (S_0) was the dominant factor, and the maximum R_a value was approximately 2.7 μm. Finally, the cumulative effect of heat was significant when DO grew from 67.7% to 82.7%, causing vaporization and a reduction in surface roughness;

(3) The apparent contact angle and roughness changes were basically consistent with those of the DO. The laser texturing and heat treatment promoted the adsorption of non-polar organic compounds, reducing the free surface energy. When the DO was greater than 55%, the surface reached the superhydrophobic state and the maximum apparent contact angle was 162.6°. However, challenges remain in the durability and stability of hydrophobic surfaces prepared by spontaneous adsorption;

(4) The stainless-steel corrosion resistance can be improved by the LST. The corrosion resistance firstly decreases, which is followed by the increase as the DO grows. When the dimples were not lapped (or slightly overlapped), the sample oxidized in the interior and the spot edge, and the passivation layer will be formed when the corrosion occurs. As the dimples continued to overlap, the effect of laser remelting deposition was intensified. Oxides located on the cluster and the oxygen-poor zone on both sides formed a micro-galvanic structure, accelerating pit corrosion and worsening the corrosion resistance. As the DO rate grew, the oxidation layers were compacted by remelting and sputtering, creating a dense passivation layer; therefore, the surface corrosion re-

sistance grew again, and the corrosion current density was 2.8×10^{-8} A·cm^{-2}, which was 4% of the original value.

References

1.　Min, J.Y.; Wan, H.L.; Carlson, B.E.; Lin, J.P.; Sun, C.C. Application of laser ablation in adhesive bonding of metallic materials: A review. *Opt. Laser Technol.* **2020**, *128*, 106188. [CrossRef]

2.　Amiriafshar, M.; Rafieazad, M.; Duan, X.L.; Nasiri, A. Fabrication and coating adhesion study of superhydrophobic stainless steel surfaces: The effect of substrate surface roughness. *Surf. Interfaces* **2020**, *20*, 11. [CrossRef]

3.　Ahmed, Y.S.; DePaiva, J.M.; Amorim, F.L.; Torres, R.D.; de Rossi, W.; Veldhuis, S.C. Laser surface texturing and characterization of austenitic stainless steel for the improvement of its surface properties. *Int. J. Adv. Manuf. Technol.* **2021**, *115*, 1795–1808. [CrossRef]

4.　Sun, K.; Yang, H.; Xue, W.; He, A.; Zhu, D.H.; Liu, W.W.; Adeyemi, K.; Cao, Y. Anti-biofouling superhydrophobic surface fabricated by picosecond laser texturing of stainless steel. *Appl. Surf. Sci.* **2018**, *436*, 263–267. [CrossRef]

5.　Yang, Z.; Liu, X.P.; Tian, Y.L. Insights into the wettability transition of nanosecond laser ablated surface under ambient air exposure. *J. Colloid Interface Sci.* **2019**, *533*, 268–277. [CrossRef]

6.　Boinovich, L.B.; Emelyanenko, A.M. The behaviour of fluoro- and hydrocarbon surfactants used for fabrication of superhydrophobic coatings at solid/water interface. *Colloids Surf. A-Physicochem. Eng. Asp.* **2015**, *481*, 167–175. [CrossRef]

7.　Boinovich, L.B.; Emelyanenko, A.M.; Emelyanenko, K.A.; Domantovsky, A.G.; Shiryaev, A.A. Comment on "Nanosecond laser textured superhydrophobic metallic surfaces and their chemical sensing applications" by Duong V. Ta, Andrew Dunn, Thomas J. Wasley, Robert W. Kay, Jonathan Stringer, Patrick J. Smith, Colm Connaughton, Jonathan D. Shephard (Appl. Surf. Sci. 357 (2015) 248–254). *Appl. Surf. Sci.* **2016**, *379*, 111–113. [CrossRef]

8.　Lou, D.Y.; Wang, B.; Liang, E.K.; Lu, G.X.; Cheng, J.; Liao, J.J.; Yang, Q.B.; Liu, D. Effect of Heat Treatment on Wettability and Condensation Heat Transfer of Laser-Textured Stainless Steel Surfaces. *Phys. Status Solidi A-Appl. Mater. Sci.* **2022**, *219*, 2100458. [CrossRef]

9.　Zhao, Z.H.; Wan, Y.; Yu, M.Z.; Wang, H.W.; Cai, Y.K.; Liu, C.; Zhang, D. Biocompability evaluation of micro textures coated with zinc oxide on Ti-6Al-4V treated by nanosecond laser. *Surf. Coat. Technol.* **2021**, *422*, 127453. [CrossRef]

10.　Tomanik, M.; Kobielarz, M.; Filipiak, J.; Szymonowicz, M.; Rusak, A.; Mroczkowska, K.; Antonczak, A.; Pezowicz, C. Laser Texturing as a Way of Influencing the Micromechanical and Biological Properties of the Poly(L-Lactide) Surface. *Materials* **2020**, *13*, 3786. [CrossRef]

11.　De Mendivil, J.M.; del Hoyo, J.; Solis, J.; Lifante, G. Ridge waveguide laser in Nd:LiNbO$_3$ by Zn-diffusion and femtosecond-laser structuring. *OptMa* **2016**, *62*, 353–356. [CrossRef]

12.　Tang, S.T.; Wang, C.; Hua, C.; Yang, L.; Wu, Y.R.; Sun, X.; Song, P.; Huang, B.X. Surface texture of substrates prepared by femtosecond laser for improving the thermal cycle life of TBCs. *Ceram. Int.* **2022**, *48*, 5775–5786. [CrossRef]

13.　Chi, G.F.; Yi, D.Q.; Liu, H.Q. Effect of roughness on electrochemical and pitting corrosion of Ti-6Al-4V alloy in 12 wt.% HCl solution at 35 °C. *J. Mater. Res. Technol.* **2020**, *9*, 1162–1174. [CrossRef]

14.　Chen, X.; Wang, F.; Di, C.X.; Zhang, C.S.; Bao, Y.L.; Tian, M.; Luo, K. Surface Morphology and Roughness Characterization of Laser Textured TC4 Titanium Alloy. *Lasers Eng.* **2021**, *48*, 349–367.

15.　Wu, Z.; Deng, J.X.; Zhang, H.; Lian, Y.S.; Zhao, J. Tribological behavior of textured cemented carbide filled with solid lubricants in dry sliding with titanium alloys. *Wear* **2012**, *292*, 135–143. [CrossRef]

16.　Rodriguez-Vidal, E.; Matthews, D.T.A.; de Viteri, V.S.; Korver, F.; Wentink, D.J.; Quintana, I. Surface design and texturing of strip steel using nanosecond pulsed lasers for simulated roughness transfer and paint appearance. *J. Mater. Process. Technol.* **2020**, *275*, 116365. [CrossRef]

17.　Kumar, V.; Verma, R.; Kango, S.; Sharma, V.S. Recent progresses and applications in laser-based surface texturing systems. *Mater. Today Commun.* **2021**, *26*, 101736. [CrossRef]

18. Zupancic, M.; Moze, M.; Gregorcic, P.; Golobic, I. Nanosecond laser texturing of uniformly and non-uniformly wettable micro structured metal surfaces for enhanced boiling heat transfer. *Appl. Surf. Sci.* **2017**, *399*, 480–490. [CrossRef]

19. Wang, Y.T.; Ke, C.J.; Wu, T.H.; Zhao, X.R.; Wang, R. Nanosecond laser texturing with hexagonal honeycomb micro-structure on Titanium for improved wettability and optical properties. *Optik* **2019**, *192*, 162953. [CrossRef]

20. Dai, G.; Chen, Y.; Lu, J.; Shen, Z.; Ni, X. Analysis of laser induced thermal mechanical relationship of HfO_2/SiO_2 high reflective optical thin film at 1064 nm. *Chin. Opt. Lett.* **2009**, *7*, 601–604.

21. Saravanan, K.G.; Thanigaivelan, R. Optimization of Laser Parameters and Dimple Geometry Using PCA-Coupled GRG. *Stroj. Vestn.-J. Mech. Eng.* **2021**, *67*, 525–533. [CrossRef]

22. Tianyu, Y.; Fengze, D.; Yongkang, Z.; Zhongwei, A.; Qingwei, W. Simulation and Experimental Study on Residual Stress Field of 2024 Aluminum Alloy Induced by Flat-Top Laser Beam. *Chin. J. Lasers* **2012**, *39*, 1003001. [CrossRef]

23. Hajnys, J.; Pagac, M.; Mesicek, J.; Petru, J.; Krol, M. Influence of Scanning Strategy Parameters on Residual Stress in the SLM Process According to the Bridge Curvature Method for AISI 316L Stainless Steel. *Materials* **2020**, *13*, 1659. [CrossRef]

24. Wang, Q.H.; Wang, H.X.; Zhu, Z.X.; Xiang, N.; Wang, Z.D.; Sun, G.F. Switchable wettability control of titanium via facile nanosecond laser-based surface texturing. *Surf. Interfaces* **2021**, *24*, 101122. [CrossRef]

25. Sirohia, G.K.; Dai, X.M. Designing air-independent slippery rough surfaces for condensation. *Int. J. Heat Mass Transf.* **2019**, *140*, 777–785. [CrossRef]

26. Li, H.; Feng, X.; Zhang, K. Study of the Classical Cassie Theory and Wenzel Theory Used in Nanoscale. *J. Bionic Eng.* **2021**, *18*, 398–408. [CrossRef]

27. Boinovich, L.B.; Emelyanenko, A.M.; Pashinin, A.S.; Lee, C.H.; Drelich, J.; Yap, Y.K. Origins of Thermodynamically Stable Superhydrophobicity of Boron Nitride Nanotubes Coatings. *Langmuir* **2012**, *28*, 1206–1216. [CrossRef]